

Article

In Situ Incorporation of TiO₂@Graphene Oxide (GO) Nanosheets in Polyacrylonitrile (PAN)-Based Membranes Matrix for Ultrafast Protein Separation

Wei Zhou ¹, Qiao Liu ^{1,2,*}, Nong Xu ², Qing Wang ², Long Fan ² and Qiang Dong ^{1,2}

¹ Hefei Tianmai Biotechnology Development Co., Ltd., No. 199 Fanhua Ave., Hefei 230601, China

² School of Energy, Materials and Chemical Engineering, Hefei University, Hefei 230601, China

* Correspondence: liuqiao@hfu.edu.cn

Abstract: Organic polymeric ultrafiltration (UF) membranes have been widely used in protein separation due to their advantages of high flux and simple manufacturing process. However, due to the hydrophobic nature of the polymer, pure polymeric UF membranes need to be modified or hybrid to increase their flux and anti-fouling performance. In this work, tetrabutyl titanate (TBT) and graphene oxide (GO) were simultaneously added to the polyacrylonitrile (PAN) casting solution to prepare a TiO₂@GO/PAN hybrid ultrafiltration membrane using a non-solvent induced phase separation (NIPS). During the phase separation process, TBT underwent a sol–gel reaction to generate hydrophilic TiO₂ nanoparticles in situ. Some of the generated TiO₂ nanoparticles reacted with the GO through a chelation interaction to form TiO₂@GO nanocomposites. The resulting TiO₂@GO nanocomposites had higher hydrophilicity than the GO. They could selectively segregate towards the membrane surface and pore walls through the solvent and non-solvent exchange during the NIPS, significantly improving the membrane’s hydrophilicity. The remaining TiO₂ nanoparticles were segregated from the membrane matrix to increase the membrane’s porosity. Furthermore, the interaction between the GO and TiO₂ also restricted the excessive segregation of the TiO₂ nanoparticles and reduced their losing. The resulting TiO₂@GO/PAN membrane had a water flux of 1487.6 L·m⁻²·h⁻¹ and a bovine serum albumin (BSA) rejection rate of 99.5%, which were much higher than those of the currently available UF membranes. It also exhibited excellent anti-protein fouling performance. Therefore, the prepared TiO₂@GO/PAN membrane has important practical applications in the field of protein separation.

Keywords: polyacrylonitrile; mixed matrix membrane; graphene oxide; titanium dioxide; ultrafiltration; protein separation

Citation: Zhou, W.; Liu, Q.; Xu, N.; Wang, Q.; Fan, L.; Dong, Q. In Situ Incorporation of TiO₂@Graphene Oxide (GO) Nanosheets in Polyacrylonitrile (PAN)-Based Membranes Matrix for Ultrafast Protein Separation. *Membranes* **2023**, *13*, 377. <https://doi.org/10.3390/membranes13040377>

Academic Editor: Cristiana Boi

Received: 2 March 2023

Revised: 21 March 2023

Accepted: 23 March 2023

Published: 26 March 2023



Copyright: © 2023 by the authors. Licensee MDPI, Basel, Switzerland. This article is an open access article distributed under the terms and conditions of the Creative Commons Attribution (CC BY) license (<https://creativecommons.org/licenses/by/4.0/>).

1. Introduction

Protein separation is a critical process in various industries, such as biological pharmacy, genetic engineering, food, and healthcare. It has therefore garnered significant attention from researchers in the field of chemical separation [1,2]. Various techniques have been traditionally used to separate proteins, such as aqueous two-phase extraction [3], gel electrophoresis [4], isoelectric precipitation [5], chromatography [6], crystallization [7], and membrane separation [8]. Among these methods, membrane separation technology is highly efficient and consumes less energy, making it an effective protein treatment method [9,10]. Additionally, it allows easy coupling and avoids destruction of the protein structure, ensuring its integrity and efficacy. Ultrafiltration (UF) is a widely used membrane separation process for protein separation and purification, which relies on size exclusion of contaminants. The mean pore size of the UF membranes is typically in the range of most protein molecules, 1 to 100 nm, making them ideal for protein separation and purification. Polyvinylidene difluoride (PVDF) [11], polysulfone (PSf) [12], polyacrylonitrile

(PAN) [13], and polyether sulfone (PES) [14] polymers are commonly used due to their excellent processability, physical and chemical resistance, thermal stability, and membrane-forming properties. However, the hydrophobic nature of these polymeric UF membranes often leads to absorption and pore blockage of protein molecules on their top surfaces, known as membrane fouling, which compromises separation performance [15,16]. To address this issue, membrane top surface hydrophilicity, pore size, and porosity can be enhanced to promote protein separation performance. Specifically, a hydrated layer barrier can be constructed on the top surface of a hydrophilic membrane to weaken the interaction between the membrane and protein molecules, inducing limited adsorption on the membrane top surface and in the large pores. Consequently, it will reduce considerable resistance during protein filtration, which will improve membrane separation properties greatly [17–23]. Various methods have been proposed, including surface grafting [24] and blending [25], to increase membrane top surface hydrophilicity. Among these, incorporating hydrophilic nanoparticles, such as graphene oxide (GO) [26], MXene [27], TiO_2 [28], and SiO_2 [29], into polymeric membrane matrices through blending or hybridization is a convenient way to improve membrane hydrophilicity. As a novel two-dimensional (2D) nanomaterial, GO has the characteristic of molecular thickness, abundant hydrophilic chemical groups ($-\text{OH}$, $-\text{O}-$, $-\text{COOH}$) on its surface and edge, as well as high mechanical strength. It has attracted a great deal of attention from researchers. Ganesh et al. dispersed the GO in the PSf membrane matrix and prepared PSf-based mixed matrix membranes (MMMs) using the non-solvent-induced phase separation (NIPS) process. This proved that GO nanosheets can greatly improve membrane hydrophilicity and salt rejection performance [30]. Lee et al. incorporated the GO nanoplates into a polymer matrix to improve the hydrophilicity and anti-fouling properties of a membrane bioreactor (MBR) [31]. Nguyen et al. blended the GO into PSf membrane matrix to enhance its hydrophilic and anti-fouling properties [32]. However, pure GO nanosheets have inadequate hydrophilicity due to their amphiphilic nature with an edge-to-center distribution of hydrophilic to hydrophobic domains [33], which makes it difficult to migrate to the membrane top surface during the NIPS. Hence, pure GO nanosheets were always modified or grafted with chemical groups and hydrophilic nanoparticles to increase their hydrophilicity. Ayyaru et al. prepared sulfonated GO nanosheets to improve PVDF membrane hydrophilicity [34]. The SiO_2 , ZnO , and TiO_2 nanoparticles were also grafted onto the surface of the GO nanosheets to increase their hydrophilicity [35–37]. Moreover, several studies have shown that, including GO nanosheets, many hydrophilic nanoparticles, such as the TiO_2 and SiO_2 , tend to migrate to the top surface of the polymeric membrane matrix during solvent and non-solvent exchanges of the NIPS, which can greatly improve membrane top surface hydrophilicity and its pore structure [38–40]. Generally, the modified GO nanosheets combined with hydrophilic nanoparticles are beneficial for improving the UF performance and anti-protein fouling performance of the membrane.

Herein, TiO_2 @GO nanosheets were synthesized in situ in the PAN membrane matrix during the NIPS formation process. TiO_2 nanoparticles, generated through the sol–gel process of the precursor, were uniformly grafted onto the top surface of the GO nanosheets. The grafting greatly improved their hydrophilicity. Most of the TiO_2 @GO nanosheets then migrated to the phase interface, including the top surface and pore wall of the membrane, resulting in significant improvements in the membrane's hydrophilicity, water flux, and anti-fouling properties. Field emission scanning electron microscopy (FESEM), Energy Dispersive X-ray Detector (EDX), Fourier Transform Infrared Spectroscopy (FTIR), and X-ray photoelectron spectroscopy (XPS) were used to characterize the membrane's morphology, element composition, and chemical structures, respectively. This work demonstrates the successful in situ generation of the TiO_2 @GO nanosheets in the PAN membrane matrix, which holds great potential for promoting the development of the GO-incorporated anti-fouling mixed matrix membranes (MMMs).

2. Experimental

2.1. Materials

Polyacrylonitrile (Purity $\geq 99.8\%$, $M_w = 15$ kDa) was purchased from Sigma-Aldrich, Shanghai, China. Flaky graphite (3000 mesh, Purity $\geq 99.5\%$) was obtained from Qingdao Chenyang Graphite Co., Ltd. (Qingdao, China). Acetic acid glacial (HAc, Purity $\geq 99.0\%$), N,N-dimethylacetamide (DMAc, Purity $\geq 99.0\%$), sulfuric acid (H_2SO_4 , Purity = 95–98%), hydrochloric acid (HCl, Purity = 36–38%), hydrogen peroxide (H_2O_2 , Purity $\geq 35.0\%$), $KMnO_4$ (Purity $\geq 99.5\%$), $K_2S_2O_8$ (Purity $\geq 99.5\%$), and P_2O_5 (Purity $\geq 99.5\%$) were all purchased from Shanghai Titan Scientific Co., Ltd. (Shanghai, China). Tetrabutyl titanate (TBT, Purity $\geq 99.0\%$) was obtained from Xilong Chemical Co., Ltd. (Chengdu, China). Bovine serum albumin (BSA, Purity = 96.0–100.0%) was purchased from Newprobo Bio-Tech Co., Ltd. (Shanghai, China). Dialysis bags (MD32, MWCO = 15,000 Da) were purchased from Spectra Medical, Inc (Shanghai, China). Deionized (DI) water was prepared by an ultra-pure water preparation machine (Pall cascada 1, Pall Corporation Shanghai, China) in our lab.

2.2. Preparation of the GO

The preparation of the GO nanosheets involved using a modified Hummers' method [41], in which 325 g flaky graphite was mixed with 15 g $K_2S_2O_8$, 15 g P_2O_5 , and 75 mL H_2SO_4 , and reacted at 80 °C for 4.5 h. The resulting graphite (pretreated powder) was obtained by washing and drying. Subsequently, 300 g dry pretreated powder was mixed with 0.65 L H_2SO_4 and 90 g $KMnO_4$ at 10 °C. After reacting at 35 °C for 2 h, 1.5 L DI water was added to the mixture with the temperature controlled below 50 °C. Next, the mixture was added to 3 L DI water and stirred for an additional 2 h. Then, 100 mL H_2O_2 (30 wt%) was added to the diluted mixture, and a golden suspended solid was obtained. Finally, the suspended solid was filtered, filled into a dialysis bag, immersed in DI water for 7 days, and the resulting GO powder was obtained by freeze-drying.

2.3. Preparation of Mixed Matrix Membranes

PAN-based MMMs were fabricated by the NIPS method. Firstly, the GO powder was added to the DMAc and ultrasonically dispersed for 1 h to prepare homogenous GO/DMAc dispersion (0.2 mg/mL). Next, the GO/DMAc dispersion, TBT (0.32 g) and HAc (2 g) were mixed and added dropwise to a PAN/DMAc solution (37.5 g, 16 wt%) under continuous stirring to create a homogenous casting solution. After removing bubbles via vacuum, the casting solution was poured onto a clean glass plate. A thin liquid film was fabricated on the plate with a scraper of 250 μ m gap. After waiting for 20 s, the glass plate was immediately immersed in DI water. The resulting membrane, denoted as GO/TiO₂/PAN, was peeled from the glass plate and stored in fresh DI water for future use. For comparison, pure PAN, GO/PAN, and TiO₂/PAN membranes were also fabricated using the same procedures without the corresponding components added (as shown in Table 1).

Table 1. Compositions of pure PAN membrane and the three kinds of PAN MMMs.

Membrane	PAN (g)	DMAc (g)	TBT (g)	GO (mg)	HAc (g)
PAN	6	42	0	0	2
GO/PAN	6	42	0	10.18	2
TiO ₂ /PAN	6	41.68	0.32	0	2
GO/TiO ₂ /PAN	6	41.68	0.32	10.18	2

2.4. Isolation of the GO in the GO/TiO₂/PAN Membrane

A piece of dry GO/TiO₂/PAN membrane was dissolved in the DMAc, producing a turbid solution. The solution was subjected to centrifugal separation using a high-speed

centrifuge at 10,000 r/min for 30 min, resulting in a brown solid at the bottom of the centrifuge tube. The solid was then dispersed in the DMAc and DI water through five additional dissolution centrifugal cycles. The resulting centrifugation product was freeze-dried to isolate the GO nanosheets.

2.5. Characterization of the Membranes

The viscosity of the casting solution was measured using the NDJ-8S rotational viscometer (Shanghai Pingxuan Scientific Instrument CO., LTD, Shanghai, China) at room temperature.

The morphology of the membrane surfaces and cross-sections was examined using an SEM (FEI-QUANTA 450, Hillsboro, OR, USA) equipped with EDX (Oxford 51-XXM0013, Abingdon, UK) capacity and FESEM (FEI-NOVA NanoSEM 450, USA). To obtain the membrane cross-section, a piece of the membrane was immersed in liquid nitrogen for 5 min and then fractured. To ensure the accurate representation of the membrane structure, five different areas of the same membrane were fractured and observed. Prior to imaging with SEM and FESEM, all samples were gold-sputtered using an EDT-2000 sputter coating instrument (USA).

The chemical structure of the membrane surface was characterized using FTIR (Thermo-Fisher 6700, Waltham, MA, USA) and XPS (Thermo-Fisher ESCALAB™ 250Xi, USA).

The hydrophilicity of the membranes was assessed with a pure water static contact angle apparatus (JC2000D, PowerEach, Shanghai, China). To minimize measurement error, the experiment was replicated five times to obtain the average results.

The overall porosity (ε) was determined using a gravimetric method, which is defined in Equation (1) [42]:

$$\varepsilon = \frac{m_1 - m_2}{A d \rho} \quad (1)$$

wherein m_1 is the weight of the wet membrane (g); m_2 is the weight of the dry membrane (g); A is the membrane area (mm²). ρ is the water density (0.998 g/cm³), and d is the membrane thickness (mm). The membrane thickness was measured using a digital micrometer.

A Thermal Gravimetric Analyzer (TGA, NETZSCH TG-209F, Selb, Germany) was used to analyze the weight loss of the MMMs in the atmosphere. The heating rate was 10 °C/min, and the final temperature was 900 °C.

A high-speed centrifuge (CENCE, TG16-WS, Changsha, China) was used to separate the GO sheets in the GO/TiO₂/PAN membrane which was dissolved in the DMAc.

2.6. Filtration and Anti-Fouling Tests

A homemade dead-end filtration equipment (Figure S1) was used to characterize the flux and rejection rate of the membrane. The detailed operating steps were as follows: A piece of round wet membrane with radius 4.5 cm was placed in the ultrafiltration cup. The feed solution, DI water or the BSA solution (1 g/L), was then poured into the cup, and the pressure was slowly decreased from 0.15 MPa (which was initially applied for 5 min using a nitrogen cylinder) to 0.1 MPa for testing. The flux of the membrane was measured and calculated with Equation (2):

$$J_w = Q / (A \Delta t) \quad (2)$$

where J_w is the flux (L·m⁻²·h⁻¹), Q is the permeating volume (L), A is the permeating area (m²), and Δt is the permeating time (h).

The anti-fouling property of the membrane was measured by a three-steps cyclic experiment under the same pressure [43]. Firstly, DI water was filtered for 50 min (J_0) in Step 1, and J_1 was measured by filtering the BSA solution for another 50 min in Step 2. After a

thorough cleaning, the measured flux of DI water was defined as J_2 in Step 3. In the second anti-fouling test, the same three steps were repeated. Based on these parameters, the flux recovery ratio (FRR), total fouling loss (R_t), reversible flux loss (R_r), and irreversible flux loss (R_{ir}) were calculated as follows:

$$FRR = \left(\frac{J_2}{J_0} \right) \times 100\% \quad (3)$$

$$R_t = \left(1 - \frac{J_1}{J_0} \right) \times 100\% \quad (4)$$

$$R_r = \left(\frac{J_2 - J_1}{J_0} \right) \times 100\% \quad (5)$$

$$R_{ir} = \left(\frac{J_0 - J_2}{J_0} \right) \times 100\% \quad (6)$$

3. Results and Discussion

3.1. Characterization of the Membranes

As shown in Figure 1, a typical asymmetric structure with a dense top skin layer, porous sub-layer, and finger-like support layer can be observed in the cross-section of all four membranes, which originated from the NIPS fabrication [44]. The big hole in the cross-section of the pure PAN membrane demonstrated the fast phase separation process of the PAN/DMAc casting solution in the NIPS, which was due to the hydrophobic nature of the PAN polymer. Finger-like pores were more likely to be observed in the PAN-based MMMs, especially for TiO₂/PAN membrane (Figure 1c), indicating that the PAN-based casting solution had a lower phase separation speed than the pure PAN casting solution. Maggay et al. demonstrated that a high viscosity of the casting solution slows down the exchange between the solvent and the non-solvent, which helps to maintain the open porous structure and interconnected pores [45]. Therefore, based on the results of viscosity tests (Figure S2), the porous sub-layer structure and straight finger-like pores (Figure 1) in the cross-sections of the PAN-based MMMs mainly originated from the high viscosities of their casting solutions. Furthermore, the interconnected finger-like pores and thin porous sub-layer of the GO/TiO₂/PAN membrane benefited the protein separation by decreasing the filtration resistance.

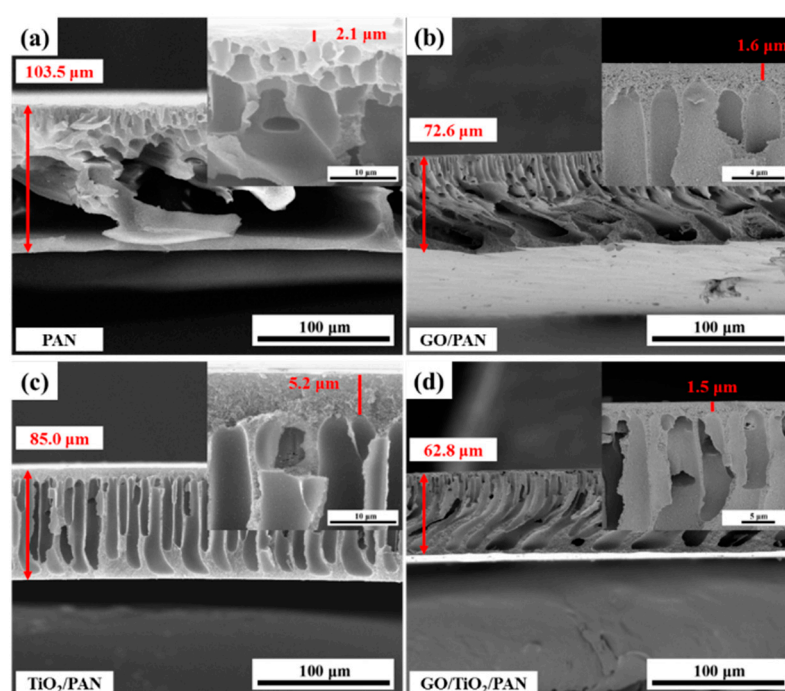


Figure 1. SEM images of the cross-sectional morphologies of the (a) PAN, (b) GO/PAN, (c) TiO₂/PAN and (d) GO/TiO₂/PAN membranes, and the amplified SEM morphologies of the four membranes' cross-sections, respectively. The area indicated by the red arrow is the area of membranes thickness measurement.

Figure 2 shows FTIR spectra of the surface of the pure PAN membrane and its MMMs. The spectra of all the membranes show the specific absorbing peaks of the PAN. The peaks at 2937 cm⁻¹, 1451 cm⁻¹, and 1370 cm⁻¹ were attributed to C–H stretching modes and in-plane bending vibration of the PAN. The peaks at 2242 cm⁻¹, 1233 cm⁻¹, and 1736 cm⁻¹ were ascribed to C≡N stretching modes, =C–H in-plane deformation vibration and C=O stretching modes of the PAN, respectively. The peaks at 1071 cm⁻¹ and 1040 cm⁻¹ were related to C–N stretching modes of the PAN, and the peak at 771 cm⁻¹ was ascribed to the skeletal vibration of $-(CH_2)_n-$. The spectra of the GO/PAN, TiO₂/PAN, and GO/TiO₂/PAN membranes show peaks with high intensity at wavenumbers ranging from 3200 cm⁻¹ to 3700 cm⁻¹, which were mainly attributed to the –OH groups originating from the incorporated GO nanosheets (as shown in Figure S3) and TiO₂ nanoparticles.

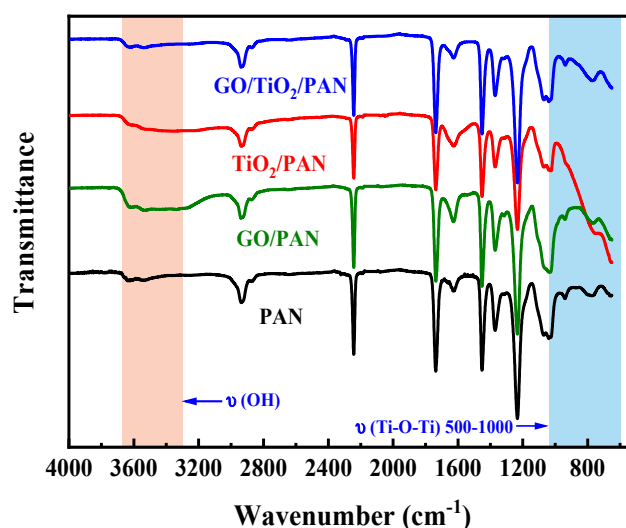


Figure 2. FTIR spectra of the PAN membrane and its MMMs.

Strong peaks at 700 cm^{-1} to 1000 cm^{-1} in the spectra of the TiO_2/PAN membrane were ascribed to the Ti-O-Ti structure [46], which demonstrates the in situ generation of the TiO_2 nanoparticles in the TiO_2/PAN membrane during the NIPS. Due to the exchange of solvent (the DMAc) and non-solvent (DI water) between membrane matrix and coagulation bath, the sol-gel reaction of TBT occurs when it comes into contact with the DI water. This forms TiO_2 nanoparticles in the membrane matrix [43]. Moreover, what's particularly interesting is that, despite the same amount of the precursor (TBT) being added to the casting solutions, higher absorption peak intensities at 700 cm^{-1} to 1000 cm^{-1} were observed in the TiO_2/PAN than in the $\text{GO}/\text{TiO}_2/\text{PAN}$ membrane.

As shown in Figure 3, the XPS data of membranes' top surfaces also indicate that TiO_2 nanoparticles were observed on the top surfaces of both the TiO_2/PAN and $\text{GO}/\text{TiO}_2/\text{PAN}$ membranes (as shown by the Ti-O-Ti peak in the O1s). A higher content of Ti was detected on the top surface of the TiO_2/PAN membrane (1.33%) than the $\text{GO}/\text{TiO}_2/\text{PAN}$ membrane (0.40%). Therefore, it is speculated that more TiO_2 nanoparticles were generated on the top surface of the TiO_2/PAN membrane than on the $\text{GO}/\text{TiO}_2/\text{PAN}$ membrane.

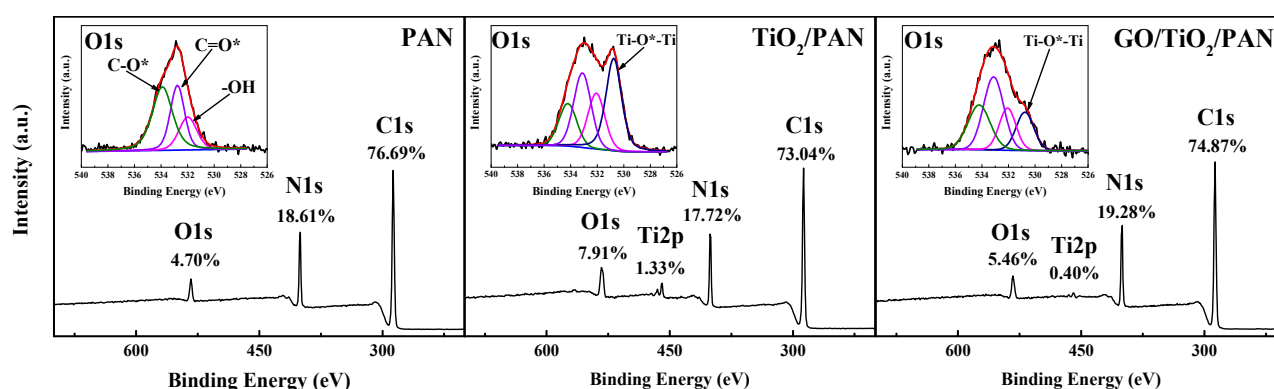


Figure 3. XPS spectra of the PAN, TiO_2/PAN and $\text{GO}/\text{TiO}_2/\text{PAN}$ membranes. * indicates the element being analyzed.

To determine the actual amount of the TiO_2 present in the entire membranes, the burnout characteristics of the TiO_2/PAN and $\text{GO}/\text{TiO}_2/\text{PAN}$ membranes were studied by TGA [47]. The TiO_2/PAN and $\text{GO}/\text{TiO}_2/\text{PAN}$ membranes were heated in air atmosphere from room temperature to $900\text{ }^{\circ}\text{C}$ at a heating rate of $10\text{ }^{\circ}\text{C}/\text{min}$. The thermal weightlessness of the GO/PAN was 99.4%, indicating that the residue should only be the TiO_2 . Table 2 shows the residual TiO_2 content in the TiO_2/PAN and $\text{GO}/\text{TiO}_2/\text{PAN}$ membranes.

As shown in Table 2, the experimental values and theoretical values of the TiO_2 in the membranes were listed. The experimental values were determined based on the TGA measurement, and the theoretical values were calculated by the Eq. 7 based on the membrane formation formula assuming complete conversion of TBT into TiO_2 . The actual contents of TiO_2 were lower than the theoretical contents in both membranes. The actual content of TiO_2 in the TiO_2/PAN membrane was higher than that in the $\text{GO}/\text{TiO}_2/\text{PAN}$ membrane. These results suggested that a portion of the in-situ-synthesized TiO_2 nanoparticles may be segregated out of the membrane matrix, which was limited by the incorporation of the GO nanosheets. Researchers have long studied the surficial migration behavior of hydrophilic nanoparticles in the polymeric membrane matrix during NIPS. According to the related research [47–49], due to the intrinsic characteristics of nanoscale size and high hydrophilicity, in-situ-generated nanoparticles tended to migrate and segregate from the polymeric membrane matrix through the exchange of the solvent and non-solvent. This induced the loss of hydrophilic nanoparticles and was unfavorable for improving the hydrophilicity of the polymeric membranes. In this study, although the incorporated GO nanosheet had high hydrophilicity, its horizontal size of 2 to $3\text{ }\mu\text{m}$ (Figure S4) made it

more difficult to segregated from the PAN-based membrane matrix than in-situ-synthesized TiO_2 nanoparticles due to the geometric size resistance. There might be interactions between the GO nanosheets and TiO_2 nanoparticles, which limited the excessive segregation of the TiO_2 nanoparticles. Therefore, the GO nanosheets in the GO/ TiO_2 /PAN membrane matrix were isolated for further characterization.

Table 2. TiO_2 content in the TiO_2 /PAN and GO/ TiO_2 /PAN membranes.

Membranes	TiO ₂ Content in the Membranes (wt%)	
	Experimental Values	Theoretical Values
TiO_2 /PAN	0.62	1.23
GO/ TiO_2 /PAN	1.07	1.24

$$\text{TiO}_2(\text{wt}\%) = \frac{W_{\text{TBT}} \times 23.48\%}{W_{\text{TBT}} \times 23.48\% + W_{\text{PAN}} + W_{\text{GO}}} \times 100\% \quad (7)$$

As shown in Figures 4a–d, nanoscale particles were uniformly distributed on the surface of the GO nanosheets, whereas the surface of the original GO nanosheets prepared by the modified Hummer's method was smooth and flat (as shown in Figures S4 and S5). In Figure 4f, Ti was detected on the surfaces of the GO nanosheets, and the C/O value (3.18) was lower than that of the original GO (5.97), indicating that TiO_2 nanoparticles were synthesized in situ on the surfaces of the GO nanosheets through the sol–gel reaction of TBT during the membrane-forming process of the NIPS. Additionally, the chemical structure of the isolated GO nanosheets were characterized using FTIR.

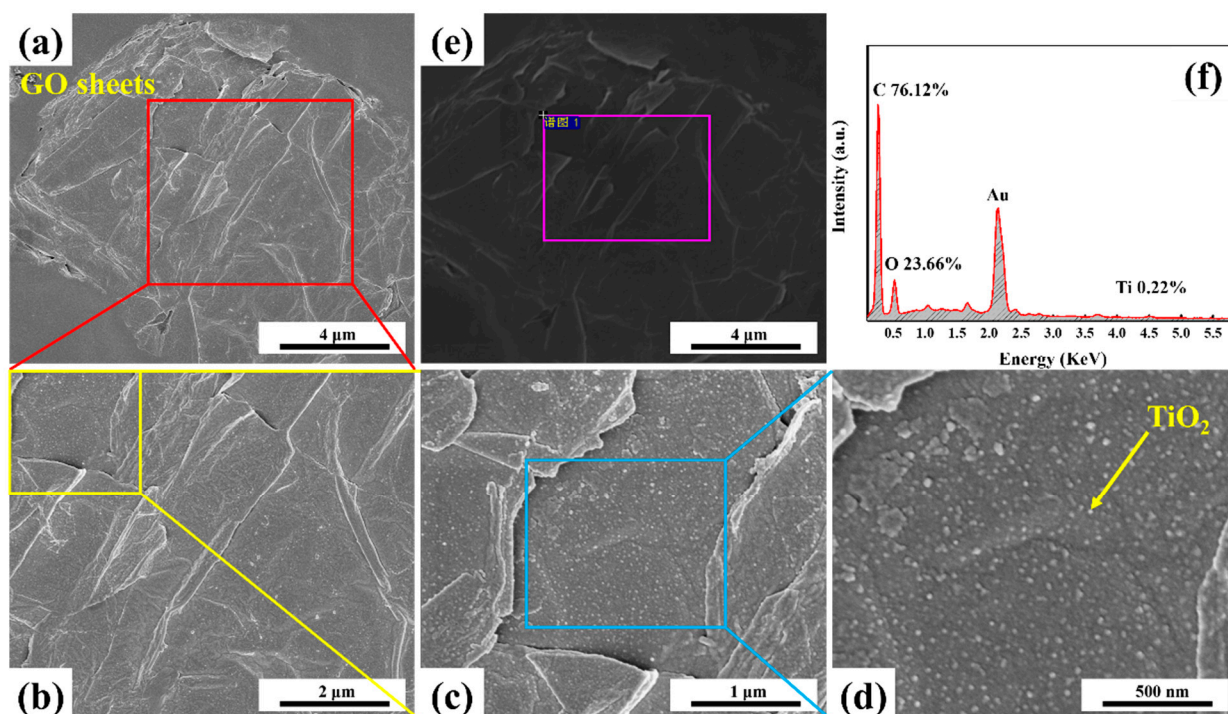


Figure 4. (a–e) FESEM images of the GO nanosheets which were isolated from the GO/ TiO_2 /PAN membranes. (f) corresponding EDX spectrum of the GO surface.

As shown in Figure 5a, the characteristic peaks at 3650 to 3100 cm^{-1} , 1730, 1627, and 1413 cm^{-1} were ascribed to $-\text{OH}$, $-\text{COOH}$, and $\text{C}=\text{O}$ stretching mode vibration of the GO nanosheets, respectively. The peaks at 1220, 1090, and 1050 cm^{-1} were attributed to $\text{C}-\text{O}-$

C stretching mode vibration of the GO nanosheets. These characteristic peaks were observed in both the GO nanosheets. However, compared to the original GO, characteristic peaks of TiO_2 at the wavenumber of 800 cm^{-1} and 500 to 1000 cm^{-1} were only observed on the surfaces of the isolated GO nanosheets, indicating the existence of TiO_2 nanoparticles on the same surface. This finding was consistent with the EDX analysis (Figure 4). Interestingly, characteristic peaks at 1458 , 1419 , 1379 , 1275 , and 1090 cm^{-1} were detected on the surfaces of the isolated GO nanosheets (Figure 5b). According to Jankovic et al.'s research, the peaks from the 1090 to 1500 cm^{-1} region were attributed to the conjugate hydroxyl structure between TiO_2 , benzoic acid, and hydroxybenzoic acid, resulting from the chelation of titanium atoms with both phenolic and carboxylic groups. [50] Hence, it is believed that TiO_2 nanoparticles were bonded to the GO by Ti atoms chelating with hydroxyl and carboxyl groups on the surface and edge of the GO nanosheets.

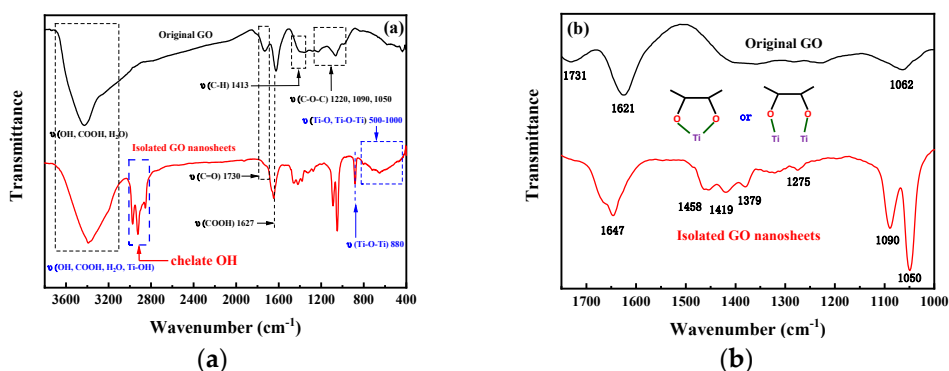


Figure 5. (a) the whole and (b) partial FTIR spectra of original prepared GO powder and isolated GO nanosheets.

Based on the above investigation, we can infer that TiO_2 nanoparticles were synthesized in situ through the sol-gel reaction of TBT during solvent and non-solvent exchanges of the NIPS. Due to the chelation of Ti atoms with hydroxyl and carboxyl groups, the in-situ-generated TiO_2 nanoparticles were loaded on the surface of the GO nanosheets (denoted as $\text{TiO}_2@\text{GO}$ nanosheets). This limited the excessive segregation of TiO_2 nanoparticles from the PAN-based membrane matrix and benefited to the improvement of membrane hydrophilicity. Additionally, the in situ loading of TiO_2 nanoparticles resulted in a higher relative content of O element in the $\text{TiO}_2@\text{GO}$ nanosheets (Figure 4f) than that of the original GO (Figure S6), indicating an increase in the number of the oxygen-containing functional groups. This enhancement of the hydrophilicity of the GO nanosheets could induce their different migration behaviors in the PAN membrane matrix.

In Figure 6a–d, scattered GO nanosheets were observed on the top surface and pore walls of the GO/PAN membrane, indicating that GO nanosheets, along with TiO_2 nanoparticles and other hydrophilic additives, migrated to the phase interfaces (top surface and pore walls) through the solvent and non-solvent exchanges [38]. Figure 6e–g show that numerous $\text{TiO}_2@\text{GO}$ nanosheets stacked layer-by-layer were observed on the top surface and pore walls of the GO/ TiO_2 /PAN membrane. This suggested that high hydrophilicity of the TiO_2 nanoparticles on the surface can provide a significant driving force for the $\text{TiO}_2@\text{GO}$ nanosheets to migrate to the membrane top surface and pore walls. To investigate the distribution of TiO_2 nanoparticles and GO nanosheets in the membrane matrix, the distributions of Ti, C, and O elements in the membrane cross-section were detected by EDX.

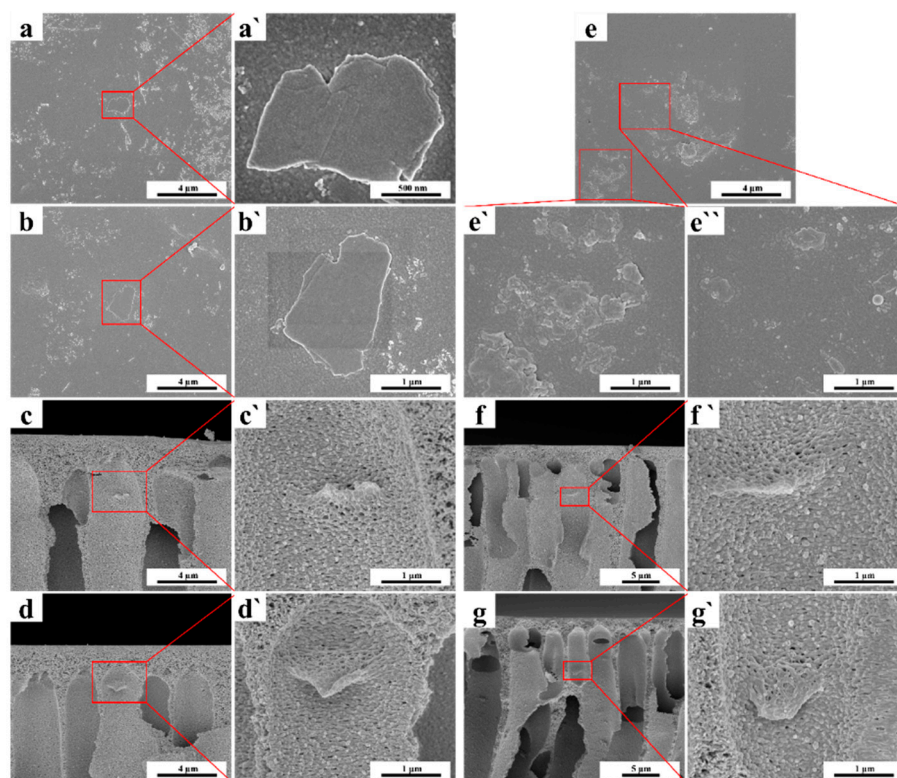


Figure 6. FESEM images of the top surfaces of (a), (a'), (b) and (b') GO/PAN membranes and (e), (e'') and (e'') GO/TiO₂/PAN membranes, and the cross-sections of (c), (c'), (d) and (d') GO/PAN membranes and (f), (f'), (g) and (g') GO/TiO₂/PAN membranes.

As shown in Figure 7, there was no obvious aggregation of C, O and Ti elements in the probability plots of the element distributions. This indicates that there was no aggregation of the GO nanosheets, in-situ-generated TiO₂ nanoparticles, or in situ formed TiO₂@GO nanocomposites within the PAN-based membrane matrix. The relative contents of C, O, N, and Ti elements in different regions of the membranes were also detected and is shown in Table 3.

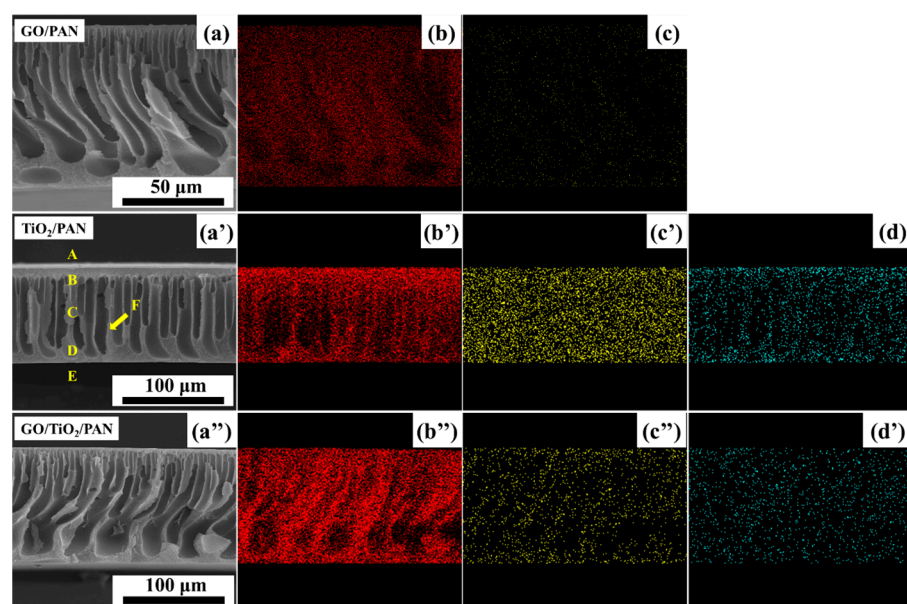


Figure 7. SEM images of the (a) GO/PAN, (a') TiO₂/PAN, and (a'') GO/TiO₂/PAN membranes' cross-sections. (b), (b'), and (b'') element C, (c), (c'), and (c'') element O and (d), (d') element Ti distribution

(points measured by EDX mapping analysis) on the membranes' cross-sections. A (top surface), B (upper wall of finger-like pore), C (middle wall of finger-like pore), D (lower wall of finger-like pore), E (bottom surface) and F (middle bulk body) were different regions in the same cross-section.

As shown in Table 3, the relative contents of C and O in the GO/PAN membrane, O and Ti in the TiO₂/PAN membrane, and C, O, and Ti in the GO/TiO₂/PAN membrane were all decreased from region A to F. The elements' relative contents in the region F for the three MMMs approximated those of the pure PAN membrane (Figure 3), demonstrating that hydrophilic additives, such as the GO nanosheets, TiO₂ nanoparticles, and the TiO₂@GO nanocomposites, all had a tendency to migrate towards the phase interfaces of their membranes. However, compared with the GO/PAN and GO/TiO₂/PAN membranes, more C and O was detected in the GO/TiO₂/PAN membrane, especially in the regions A and B. This implies that surficial migration happened in most of the TiO₂@GO nanocomposites because of their high hydrophilicity, which was also consistent with the results of FESEM (Figure 6).

Table 3. Relative content of C, O, N, and Ti in different regions of the GO/PAN, TiO₂/PAN, and GO/TiO₂/PAN MMMs.

Region	GO/PAN (%)			TiO ₂ /PAN (%)			GO/TiO ₂ /PAN (%)				
	C	O	N	C	O	N	Ti	C	O	N	Ti
A	77.33	5.12	17.55	73.12	7.88	17.65	1.35	78.71	6.42	14.46	0.55
B	77.08	4.97	17.95	73.44	7.62	17.73	1.21	78.66	6.21	14.62	0.51
C	76.95	4.91	18.14	74.29	6.75	17.93	1.03	78.47	6.07	15.02	0.44
D	76.90	4.88	18.22	76.00	5.12	18.34	0.54	78.16	5.87	15.61	0.36
E	76.87	4.82	18.31	76.40	4.85	18.44	0.31	77.95	5.65	16.12	0.28
F	76.85	4.70	18.45	76.70	4.66	18.52	0.12	77.19	5.13	17.58	0.10

Generally, the in-situ-generated TiO₂ nanoparticles and the GO nanosheets influenced each other's surficial migration behavior during the GO/TiO₂/PAN membrane fabrication. The formation process and mechanism of their interactions are illustrated in Figure 8.

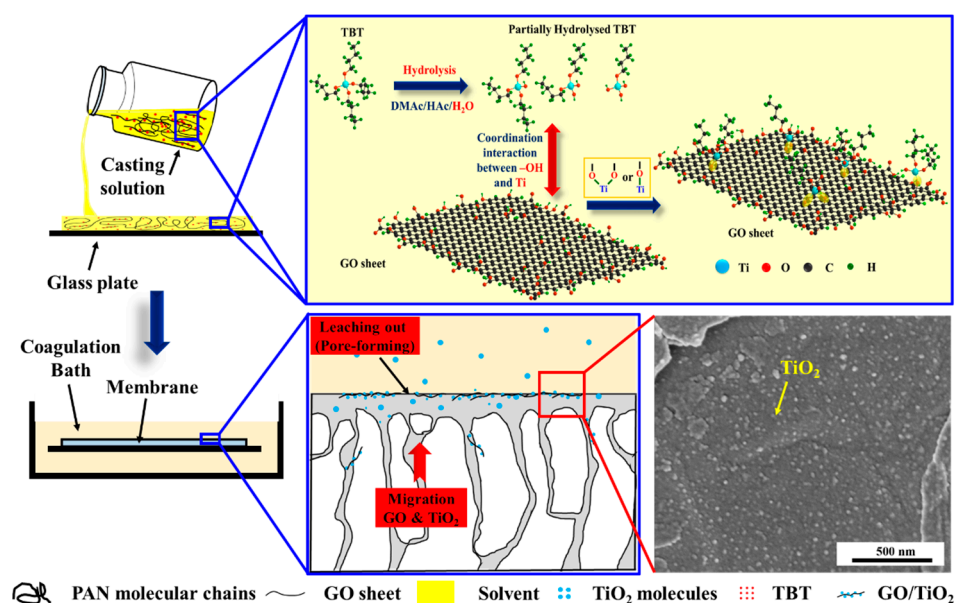


Figure 8. The schematic diagram of the membrane forming mechanism of the GO/TiO₂/PAN membrane and the synergistic effects between the GO nanosheets and TiO₂ nanoparticles.

First, a homogenous PAN/TBT/GO/DMAc solution was cast onto a clean glass plate to form a liquid film. Once the film was immersed in DI water, the membrane formation (the NIPS process) occurred. Initially, due to the good intersolubility of the solvent (the DMAc) and non-solvent (water), the DMAc in the liquid film dissolved into water gradually, breaking the thermodynamic equilibrium of the liquid film. This resulted in the differentiation of the original homogenous casting solution into a polymer-rich region and a polymer-poor region [51]. The polymer-rich region mainly comprised the PAN, GO nanosheet, TBT, and a small amount of the DMAc, while most of the DMAc and water were incorporated into the polymer-poor region. The two regions were separated due to the difference in density. The polymer-poor region was gathered in the polymer matrix, creating phase interfaces between the two regions, membrane top surface and pore walls. With the exchange of the DMAc and water between the polymer-poor region and coagulation bath, the water concentration of the polymer-poor region increased, providing opportunities for the contact of the GO nanosheets, TBT, and water. It not only created the conditions for the in situ generation of TiO₂ nanoparticles but also induced the surficial migration of the GO and TiO₂ before the polymer-rich region cured in membrane matrix. Importantly, because of the strong chelating interaction between Ti atoms and the GO nanosheets, most of the in-situ-generated TiO₂ nanoparticles were bonded to the surface of the GO (TiO₂@GO nanocomposites). This limited the excessive migration of TiO₂, reduced the loss of the hydrophilic nanoparticles, and promoted the surficial migration of the TiO₂@GO nanocomposites. According to Chen et al.'s research, physical incompatibilities between the PAN and inorganic materials probably loosened the skin layer of the generated membrane [47]. TiO₂ nanoparticles with nanoscale size can leach from the top-layer and pore walls into the coagulation bath (pore-forming agent) and can greatly increase membrane porosity [47,52]. However, due to the big horizontal size (Figure S4) and high hydrophilicity, most of the TiO₂@GO nanocomposites migrate to the top surface and pore walls of the GO/TiO₂/PAN MMMs, which may greatly enhance the membrane hydrophilicity.

3.2. Permeability and Anti-Fouling Properties of the Membranes

As shown in Figure 9a, the pure PAN membrane had the highest water contact angle (WCA) and the lowest overall porosity among the four tested membranes. The WCA decreased from PAN to GO/TiO₂/PAN membrane, while the overall porosity increased. The GO/TiO₂/PAN MMM with WCA of 40.4° and overall porosity of 88.8% had the best hydrophilicity and porous structure among them. Several studies have shown that hydrophilic additives in a polymer matrix lead to faster phase separation [53–55]. When combined with the leaching of TiO₂ nanoparticles, this resulted in a highly porous membrane [38]. Additionally, due to the surficial migration behavior of the GO, TiO₂, and TiO₂@GO nanomaterials, the hydrophilicity of the MMMs' top surfaces was greatly improved, especially that of the TiO₂@GO nanocomposites in the GO/TiO₂/PAN MMM. Generally, high porosity reduced the filtration resistance of the membranes, and a hydrophilic membrane top surface resisted the absorption of various protein molecules, which was conducive to enhancing the filtration and anti-fouling performance of all PAN-based membranes.

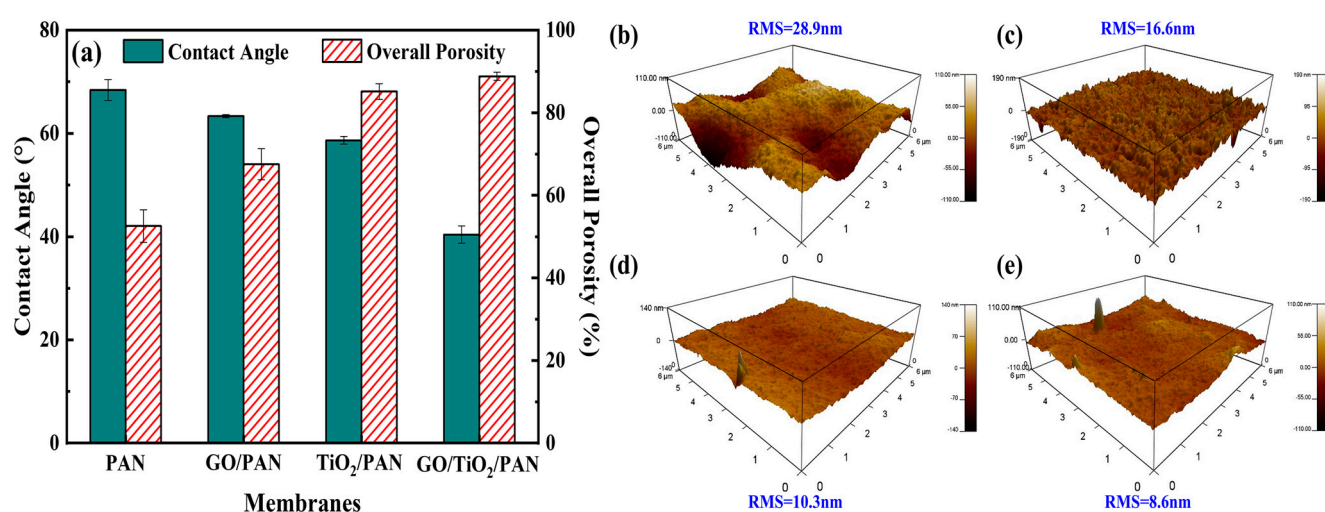


Figure 9. (a) contact angle and overall porosity of the PAN, GO/PAN, TiO₂/PAN, and GO/TiO₂/PAN MMMs, 3D AFM images and mean roughness of the (b) PAN, (c) GO/PAN, (d) TiO₂/PAN, and (e) GO/TiO₂/PAN MMMs top surface.

Surface roughness, which greatly influences membrane anti-fouling performance during protein separation, was also detected. In Figure 9b, the pure PAN had the highest mean surface roughness of 28.9 nm. Big “valleys” and “peaks” were observed on the top surface, creating favorable conditions for hiding the protein on the membrane surface. This made it difficult for the absorbed protein to be washed away. However, the surface roughness of all PAN-based MMMs was lower than that of the pure PAN membrane, especially for the GO/TiO₂/PAN MMM. According to the mechanism of the NIPS process, the rough morphology of the top-layer was mainly attributed to the rapid diffusional exchange of solvent for non-solvent in the top-layer. This led to the vitrification of the maxima of the concentration fluctuations that formed the nodules, namely polymer nodular structure [56,57]. Slow phase separation process of the polymer could limit the generation of polymer nodular and fabricate a smooth top surface of the membrane. [58] From the kinetics perspective, an increase in the viscosity of the casting solution, caused by the addition of the GO nanosheets, TiO₂ nanoparticles, and TiO₂@GO nanocomposites (Figure S2), raised the number of molecules per unit volume and restricted the molecules’ motion, resulting in a slowdown of the phase inversion rate. Although many studies have shown that the addition of hydrophilic nanoparticles in the polymeric membrane matrix could increase the membrane surface roughness [59–61], the surface roughness of the MMMs was greatly influenced by the aggregation state of the nanoparticles [62,63]. Hence, it could be inferred that the GO nanosheets did not have better distribution state than the in-situ-generated TiO₂ nanoparticles in the PAN matrix. The TiO₂ on the surface of the GO could promote dispersion of the TiO₂@GO nanocomposites, inducing the smooth top surface of the GO/TiO₂/PAN MMM. The smoother surface always exhibited a lower irreversible attachment of the foulants on the membrane top surface, a higher flux recovery and better anti-fouling property [63,64]. These were analyzed by the BSA rejection and anti-fouling tests as shown in Figures 10 and 11.

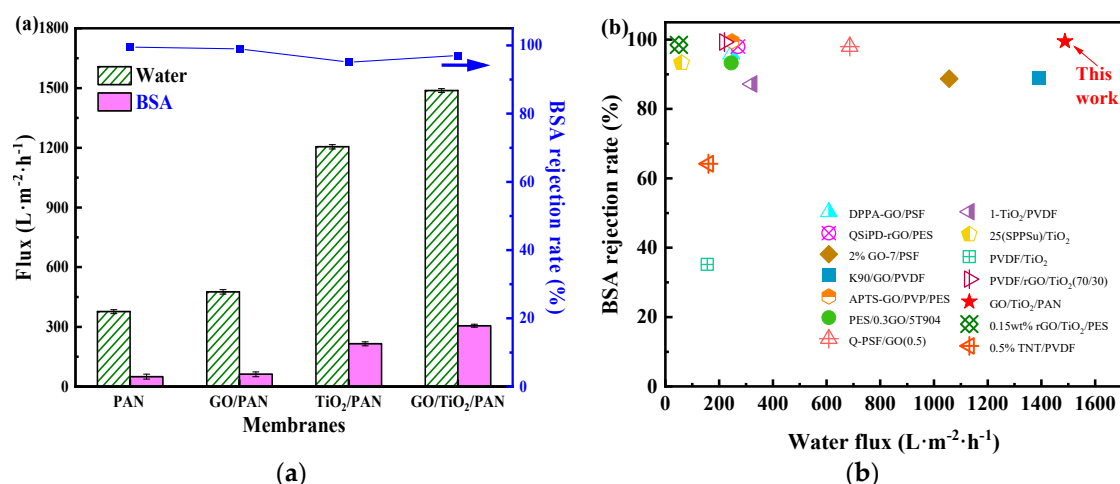


Figure 10. (a) Pure water flux and BSA rejection rate of the PAN, GO/PAN, TiO_2/PAN and $\text{GO}/\text{TiO}_2/\text{PAN}$ membranes, (b) Comparison of the filtration performance in current work with others.

In Figure 10a, pure water fluxes of the MMMs were higher than those of the pure PAN membrane ($376.9 \text{ L} \cdot \text{m}^{-2} \cdot \text{h}^{-1}$). The $\text{GO}/\text{TiO}_2/\text{PAN}$ membranes, in particular, exhibited a pure water flux of $1487.6 \text{ L} \cdot \text{m}^{-2} \cdot \text{h}^{-1}$, which was nearly four times higher than that of the PAN membrane. The pure PAN membrane could reject 99.5% of the BSA molecules in the feeding solution, indicating that the mean pore size of the membrane top surface was less than 8.0 nm and could be classified as a UF membrane [65]. Moreover, although the pure water flux of the MMMs was greatly improved, their BSA rejection rates were still higher than 95%, implying that the mean pore sizes of the membranes top surfaces were not altered by the incorporation of the GO and TiO_2 . Furthermore, the filtration properties of the $\text{GO}/\text{TiO}_2/\text{PAN}$ MMM were compared with other MMMs mainly incorporating the GO and/or TiO_2 [26,37,66–75]. As shown in Figure 10b and Table S1, the fabricated $\text{GO}/\text{TiO}_2/\text{PAN}$ MMM, with a pure water flux and BSA rejection rate of $1487.6 \text{ L} \cdot \text{m}^{-2} \cdot \text{h}^{-1}$ and 99.5%, respectively, had the best UF properties compared with others. Therefore, the $\text{GO}/\text{TiO}_2/\text{PAN}$ MMM exhibited great potential for application in protein separation.

The anti-fouling performances of the membranes, which were important for the application prospects of the UF membranes, were also analyzed by a three-step cyclic anti-fouling test.

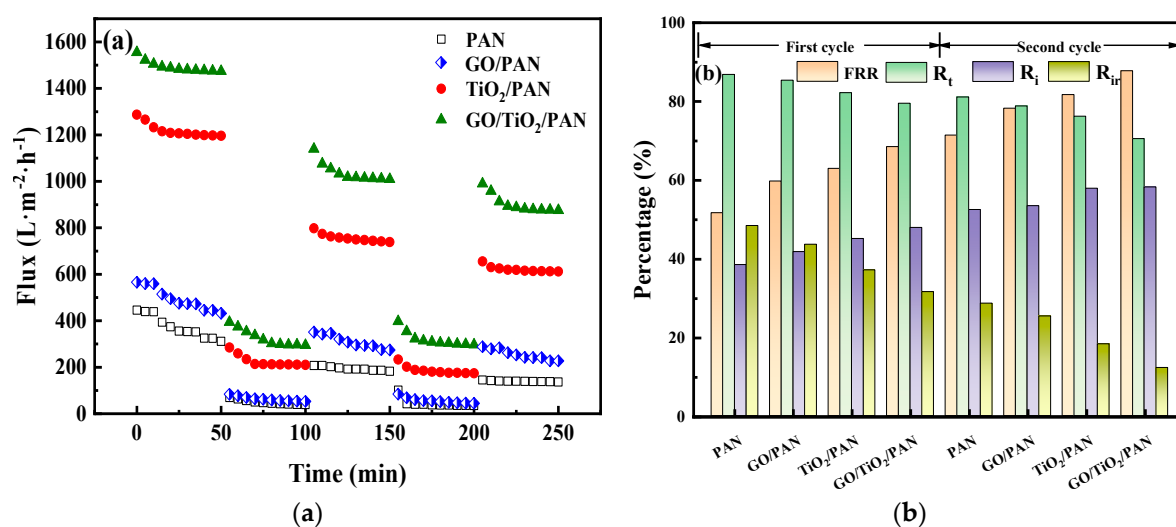


Figure 11. (a) Flux variations of the PAN, GO/PAN, TiO_2/PAN , and $\text{GO}/\text{TiO}_2/\text{PAN}$ membranes during the three-step filtration cycles with two curves of the BSA results, (b) FRR, R_i , R_{ir} , and R_t of the PAN, GO/PAN, TiO_2/PAN , and $\text{GO}/\text{TiO}_2/\text{PAN}$ membranes in the two filtration circles.

As shown in Figure 11a, the pure water fluxes of the membranes decreased slightly in the first 50 min, likely due to the membrane compaction at 0.15 MPa prior to the measurement. However, when the feed liquid was changed to the BSA solution, the flux decreased sharply because of the deposition and adsorption of the protein on the membrane top surface. After washing, the water flux was still less than the initial value, indicating that some proteins on the membranes' top surface could not be fully washed away. In the second filtration cycle, the water flux did not reduce significantly, possibly due to the dynamic equilibrium of the absorption and desorption (washing) of the BSA molecules on the membrane surface.

Anti-fouling parameters were calculated using Equations (3)–(6), and the results are presented in Figure 11b and Table S2. It can be seen that the FRR and R_i increased, while the R_t and R_{ir} decreased, from the PAN, GO/PAN, TiO_2 /PAN, and GO/ TiO_2 /PAN membranes in the two anti-fouling cycles. This suggests that the absorbed BSA molecules on the GO/ TiO_2 /PAN membrane top surface were more easily washed away than those on the other three. As discussed in Figure 9, the high hydrophilicity and smooth surface of the GO/ TiO_2 /PAN membrane ensured that the protein molecules were not easily absorbed on its top surface. The absorbed protein molecules were easily washed away, thereby endowing the membrane with excellent anti-fouling performance.

Moreover, the FRR and R_i were higher and the R_t and R_{ir} were lower in the second cycle than those in the first cycle, indicating that better anti-fouling performance was exhibited in the second cycle than in the first cycle for the same kinds of membranes. In practice, the adsorption and desorption of the protein molecules on the membranes' top surfaces were in dynamic equilibrium. Therefore, the anti-fouling parameters in the second cycle could be used to characterize the real anti-fouling performances of the membranes. Compared with other research, the FRR of the GO/ TiO_2 /PAN membrane (87.74%) was higher than most of the reported results [13,16,60,71–76].

4. Conclusions

In this work, inorganic nanoparticle precursor (TBT) and the GO were added to the PAN casting solution to prepare a UF membrane with the TiO_2 @GO/PAN mixed matrix using the NIPS. During the phase separation process, TBT underwent the sol–gel reaction to generate hydrophilic TiO_2 nanoparticles in situ. Some of the generated TiO_2 nanoparticles formed the TiO_2 @GO nanocomposites through chelation interactions with the GO. The generated TiO_2 @GO nanocomposites had higher hydrophilicity than the GO, and could bias towards the membrane surface and pore walls through the exchange between the solvents and non-solvents during the NIPS process, significantly improving the hydrophilicity of the membrane. Another part of the TiO_2 nanoparticles was biased against the membrane body by exchanging the solvents and non-solvents, improving the porosity of the membrane. In addition, the interaction between the GO and TiO_2 limited the excessive segregation of TiO_2 nanoparticles, reducing the loss of TiO_2 nanoparticles. Generally, the interaction between the GO and TiO_2 significantly improved the hydrophilicity and porosity of the PAN matrix. The water flux and BSA retention of the prepared TiO_2 @GO/PAN MMM were $1487.6 \text{ L}\cdot\text{m}^{-2}\cdot\text{h}^{-1}$ and 99.5%, respectively, which was much higher than the performances of current mixed matrix UF membranes. The FRR and R_i were 87.74% and 70.47%, respectively, demonstrating its excellent anti-fouling properties. Moreover, considering the only solvent of BSA molecules, additional work will be done for a fuller characterization of the membrane at a wide range of concentrations, pHs, conductivities, etc. to test the applicability of the current membrane construction to real applications.

Supplementary Materials: The following supporting information can be downloaded at: <https://www.mdpi.com/article/10.3390/membranes13040377/s1>, Figure S1: Schematic diagram of the homemade dead-end filtration equipment in filtration and anti-fouling tests, Figure S2: Casting solutions' viscosity of the PAN, GO/PAN, TiO_2 /PAN and GO/ TiO_2 /PAN membranes, Figure S3: FTIR

of the prepared GO nanosheets, Figure S4: AFM images and curves of the horizontal cross sections of the prepared GO nanosheets, Figure S5: TEM images of the prepared GO nanosheets, Figure S6: (a) FESEM images of the original GO nanosheets prepared by the modified Hummer's method. (b) corresponding EDX spectrum of the GO nanosheet's surface, Figure S7: XRD curve of the prepared GO nanosheets, Table S1: Comparison of the UF performance with others, Table S2: Anti-fouling parameters of the PAN, GO/PAN, TiO₂/PAN and GO/TiO₂/PAN membranes in cyclic anti-fouling tests. References [65–76] are cited in the Supplementary Materials.

Author Contributions: Conceptualization, Q.L. and W.Z.; methodology, Q.L.; software, Q.L.; validation, W.Z., Q.L. and N.X.; formal analysis, Q.L.; investigation, W.Z. and Q.L.; resources, Q.L., N.X., Q.W. and L.F.; data curation, W.Z. and Q.L.; writing—original draft preparation, Q.L. and W.Z.; writing—review and editing, Q.L., N.X. and L.F.; visualization, Q.L.; supervision, Q.L. and N.X.; project administration, Q.L., N.X., L.F. and Q.D.; funding acquisition, Q.L., N.X., Q.W. and L.F. All authors have read and agreed to the published version of the manuscript.

Funding: This work was funded by Key Research and Development Project of Anhui Province, China (2022a05020041), University Natural Sciences Research Project of Anhui Province (KJ2020A0669, KJ2021A1015)

Acknowledgments: This work was also supported by Open Funding Project of the State Key Laboratory of Biochemical Engineering, IPE, CAS. The authors would like to thank Suzhou Deyo Bot Advanced Materials Co., Ltd. for its support of material characterization.

Conflicts of Interest: The authors declare no conflict of interest.

Abbreviations

2D	Two-dimensional
BSA	Bovine serum albumin
DI	Deionized
DMAc	N, N-dimethylacetamide
EDX	Energy dispersive X-ray detector
FESEM	Field emission scanning electron microscopy
FRR	Flux recovery ratio
FTIR	Fourier transform infrared spectroscopy
GO	Graphene oxide
HAc	Acetic acid
MBR	Membrane bio-reactor
MMMs	Mixed matrix membranes
NIPS	Non-solvent induced phase separation
PAN	Polyacrylonitrile
PES	Polyether sulfone
PSf	Polysulfone
PVDF	Polyvinyl difluoride
R _{ir}	Irreversible flux loss
R _r	Reversible flux loss
R _t	Total fouling loss
TBT	Tetrabutyl titanate
UF	Ultrafiltration
WCA	Water contact angle
XPS	X-ray photoelectron spectroscopy

References

1. Liu, S.; Li, Z.; Yu, B.; Wang, S.; Shen, Y.; Cong, H. Recent advances on protein separation and purification methods. *Adv. Colloid Interface Sci.* **2020**, *284*, 102254. <https://doi.org/10.1016/j.cis.2020.102254>.
2. Smith, D.M. Protein separation and characterization procedures. In *Food Analysis*; Food Science Text Series; Nielsen, S.S., Ed.; Springer: Cham, Switzerland, 2017; pp. 431–453.

3. Asenjo, J.A.; Andrews, B.A. Aqueous two-phase systems for protein separation: A perspective. *J. Chromatogr. A* **2011**, *1218*, 8826–8835. <https://doi.org/10.1016/j.chroma.2011.06.051>.
4. Zhu, Z.; Lu, J.J.; Liu, S. Protein separation by capillary gel electrophoresis: A review. *Anal. Chim. Acta* **2012**, *709*, 21–31. <https://doi.org/10.1016/j.aca.2011.10.022>.
5. Thekkilaveedu, S.; Krishnaswami, V.; Mohanan, D.P.; Alagarsamy, S.; Natesan, S.; Kandasamy, R. Lactic acid-mediated isolation of alpha-, beta- and kappa-casein fractions by isoelectric precipitation coupled with cold extraction from defatted cow milk. *Int. J. Dairy Technol.* **2020**, *73*, 31–39.
6. Li, B.; Guo, F.; Hu, H.; Liu, P.; Tan, M.J.; Pan, J.Y.; Zhai, L.H. The characterization of column heating effect in nanoflow liquid chromatography mass spectrometry (nanoLC-MS)-based proteomics. *J. Mass Spectrom.* **2020**, *55*, e4441.
7. Mathew, T.K.; Lakerveld, R. An airlift crystallizer for protein crystallization. *Ind. Eng. Chem. Res.* **2019**, *58*, 20381–20391.
8. Chen, G.; Song, W.; Qi, B.; Ghosh, R.; Wan, Y. Separation of human serum albumin and polyethylene glycol by electro-ultrafiltration. *Biochem. Eng. J.* **2016**, *109*, 127–136.
9. Chai, M.; Ye, Y.; Chen, V. Separation and concentration of milk proteins with a submerged membrane vibrational system. *J. Membr. Sci.* **2016**, *524*, 305–314. <https://doi.org/10.1016/j.memsci.2016.11.043>.
10. Ding, L.; Zhang, W.; Ould-Dris, A.; Jaffrin, M.Y.; Tang, B. Concentration of Milk Proteins for Producing Cheese Using a Shear-Enhanced Ultrafiltration Technique. *Ind. Eng. Chem. Res.* **2016**, *55*, 11130–11138. <https://doi.org/10.1021/acs.iecr.6b02738>.
11. Saraswathi, M.S.S.A.; Rana, D.; Kaleekkal, N.J.; Divya, K.; Nagendran, A. Investigating the efficacy of PVDF membranes customized with sulfonated graphene oxide nanosheets for enhanced permeability and antifouling. *J. Environ. Chem. Eng.* **2020**, *8*, 104426. <https://doi.org/10.1016/j.jece.2020.104426>.
12. Lavanya, C.; Balakrishna, R.G. Naturally derived polysaccharides-modified PSF membranes: A potency in enriching the anti-fouling nature of membranes. *Sep. Purif. Technol.* **2020**, *230*, 115887.
13. Jiang, L.; Yun, J.; Wang, Y.; Yang, H.; Xu, Z.; Xu, Z.-L. High-flux, anti-fouling dendrimer grafted PAN membrane: Fabrication, performance and mechanisms. *J. Membr. Sci.* **2019**, *596*, 117743. <https://doi.org/10.1016/j.memsci.2019.117743>.
14. Al-Ghafri, B.; Kyaw, H.H.; Al-Abri, M.; Lau, W.-J. Performance study of novel PES membrane using electrospray deposition method for organic contaminants separation. *Chem. Eng. Res. Des.* **2022**, *186*, 73–81. <https://doi.org/10.1016/j.cherd.2022.07.028>.
15. Shi, X.; Tal, G.; Hankins, N.P.; Gitis, V. Fouling and cleaning of ultrafiltration membranes: A review. *J. Water Process. Eng.* **2014**, *1*, 121–138. <https://doi.org/10.1016/j.jwpe.2014.04.003>.
16. Feng, H.; Liu, J.; Mu, Y.; Lu, N.; Zhang, S.; Zhang, M.; Luan, J.; Wang, G. Hybrid ultrafiltration membranes based on PES and MOFs @ carbon quantum dots for improving anti-fouling performance. *Sep. Purif. Technol.* **2021**, *266*, 118586. <https://doi.org/10.1016/j.seppur.2021.118586>.
17. Wang, Z.; Ji, S.; He, F.; Cao, M.; Peng, S.; Li, Y. One-step transformation of highly hydrophobic membranes into superhydrophilic and underwater superoleophobic ones for high-efficiency separation of oil-in-water emulsions. *J. Mater. Chem. A* **2018**, *6*, 3391–3396.
18. Zarghami, S.; Mohammadi, T.; Sadrzadeh, M.; Van der Bruggen, B. Bio-inspired anchoring of amino-functionalized multi-wall carbon nanotubes (N-MWCNTs) onto PES membrane using polydopamine for oily wastewater treatment. *Sci. Total. Environ.* **2019**, *711*, 134951. <https://doi.org/10.1016/j.scitotenv.2019.134951>.
19. Rohani, M.M.; Mehta, A.; Zydney, A.L. Development of high performance charged ligands to control protein transport through charge-modified ultrafiltration membranes. *J. Membr. Sci.* **2010**, *362*, 434–443. <https://doi.org/10.1016/j.memsci.2010.06.069>.
20. Liu, Y.; Yue, X.; Zhang, S.; Ren, J.; Yang, L.; Wang, Q.; Wang, G. Synthesis of sulfonated polyphenylsulfone as candidates for antifouling ultrafiltration membrane. *Sep. Purif. Technol.* **2012**, *98*, 298–307. <https://doi.org/10.1016/j.seppur.2012.06.031>.
21. Li, Y.; Chung, T.-S. Exploration of highly sulfonated polyethersulfone (SPES) as a membrane material with the aid of dual-layer hollow fiber fabrication technology for protein separation. *J. Membr. Sci.* **2008**, *309*, 45–55. <https://doi.org/10.1016/j.memsci.2007.10.006>.
22. Li, Y.; Soh, S.C.; Chung, T.-S.; Chan, S.Y. Exploration of ionic modification in dual-layer hollow fiber membranes for long-term high-performance protein separation. *AIChE J.* **2008**, *55*, 321–330. <https://doi.org/10.1002/aic.11671>.
23. Kim, D.-G.; Kang, H.; Han, S.; Lee, J.-C. The increase of antifouling properties of ultrafiltration membrane coated by star-shaped polymers. *J. Mater. Chem.* **2012**, *22*, 8654–8661. <https://doi.org/10.1039/c2jm16439f>.
24. Yang, X.; Zhang, B.; Liu, Z.; Deng, B.; Yu, M.; Jiang, H.; Li, J. Preparation of the antifouling microfiltration membranes from poly (N, N-dimethylacrylamide) grafted poly (vinylidene fluoride) (PVDF) powder. *J. Mater. Chem.* **2011**, *21*, 11908–11915.
25. Wang, H.; Wang, W.; Wang, L.; Zhao, B.; Zhang, Z.; Xia, X.; Yang, H.; Xue, Y.; Chang, N. Enhancement of hydrophilicity and the resistance for irreversible fouling of polysulfone (PSF) membrane immobilized with graphene oxide (GO) through chloromethylated and quaternized reaction. *Chem. Eng. J.* **2017**, *334*, 2068–2078. <https://doi.org/10.1016/j.cej.2017.11.135>.
26. Han, R.; Ma, X.; Xie, Y.; Teng, D.; Zhang, S. Preparation of a new 2D MXene/PES composite membrane with excellent hydrophilicity and high flux. *Rsc Adv.* **2017**, *7*, 56204–56210.
27. Méricq, J.P.; Mendret, J.; Brosillon, S.; Faur, C. High performance PVDF-TiO₂ membranes for water treatment. *Chem. Eng. Sci.* **2015**, *123*, 283–291.
28. Shen, J.-N.; Ruan, H.-M.; Wu, L.-G.; Gao, C.-J. Preparation and characterization of PES-SiO₂ organic-inorganic composite ultrafiltration membrane for raw water pretreatment. *Chem. Eng. J.* **2011**, *168*, 1272–1278. <https://doi.org/10.1016/j.cej.2011.02.039>.
29. Ganesh, B.M.; Isloor, A.M.; Ismail, A.F. Enhanced hydrophilicity and salt rejection study of graphene oxide-polysulfone mixed matrix membrane. *Desalination* **2013**, *313*, 199–207. <https://doi.org/10.1016/j.desal.2012.11.037>.

30. Lee, J.; Chae, H.-R.; Won, Y.J.; Lee, K.; Lee, C.-H.; Lee, H.H.; Kim, I.-C.; Lee, J.-M. Graphene oxide nanoplatelets composite membrane with hydrophilic and antifouling properties for wastewater treatment. *J. Membr. Sci.* **2013**, *448*, 223–230. <https://doi.org/10.1016/j.memsci.2013.08.017>.
31. Nguyen, H.T.V.; Ngo, T.H.A.; Do, K.D.; Nguyen, M.N.; Dang, N.T.T.; Nguyen, T.T.H.; Vien, V.; Vu, T.A. Preparation and Characterization of a Hydrophilic Polysulfone Membrane Using Graphene Oxide. *J. Chem.* **2019**, *2019*, 3164373. <https://doi.org/10.1155/2019/3164373>.
32. Zinadini, S.; Zinatizadeh, A.A.; Rahimi, M.; Vatanpour, V.; Zangeneh, H. Preparation of a novel antifouling mixed matrix PES membrane by embedding graphene oxide nanoplates. *J. Membr. Sci.* **2014**, *453*, 292–301. <https://doi.org/10.1016/j.memsci.2013.10.070>.
33. Razmjou, A.; Resosudarmo, A.; Holmes, R.L.; Mansouri, J.; Chen, V. The effect of modified TiO₂ nanoparticles on the polyethersulfone ultrafiltration hollow fiber membranes. *Desalination* **2012**, *287*, 271–280.
34. Yu, S.; Zuo, X.; Bao, R.; Xu, X.; Wang, J.; Xu, J. Effect of SiO₂ nanoparticle addition on the characteristics of a new organic–inorganic hybrid membrane. *Polymer* **2009**, *50*, 553–559. <https://doi.org/10.1016/j.polymer.2008.11.012>.
35. Xie, Q.; Zhang, S.; Ma, H.; Shan, W.; Gong, X.; Zhuan, H. A novel thin-film nanocomposite nanofiltration membrane by incorporating 3D hyperbranched polymer functionalized 2D graphene oxide. *Polymers* **2018**, *10*, 1253.
36. Ayyaru, S.; Ahn, Y.-H. Application of sulfonic acid group functionalized graphene oxide to improve hydrophilicity, permeability, and antifouling of PVDF nanocomposite ultrafiltration membranes. *J. Membr. Sci.* **2017**, *525*, 210–219. <https://doi.org/10.1016/j.memsci.2016.10.048>.
37. Zhu, Z.; Jiang, J.; Wang, X.; Huo, X.; Li, Q.; Wang, L. Improving the hydrophilic and antifouling properties of polyvinylidene fluoride membrane by incorporation of novel nanohybrid GO@SiO₂ particles. *Chem. Eng. J.* **2017**, *314*, 266–276.
38. Mahlangu, O.T.; Nackaerts, R.; Thwala, J.M.; Manba, B.B.; Verliefde, A.R.D. Hydrophilic fouling-resistant GO-ZnO/PES membranes for wastewater reclamation. *J. Membr. Sci.* **2017**, *524*, 43–55.
39. Safarpour, M.; Vatanpour, V.; Khataee, A. Preparation and characterization of graphene oxide/TiO₂ blended PES nanofiltration membrane with improved antifouling and separation performance. *Desalination* **2015**, *393*, 65–78. <https://doi.org/10.1016/j.desal.2015.07.003>.
40. Alam, S.N.; Sharma, N.; Kumar, L. Synthesis of Graphene Oxide (GO) by Modified Hummers Method and Its Thermal Reduction to Obtain Reduced Graphene Oxide (rGO)*. *Graphene* **2017**, *6*, 1–18. <https://doi.org/10.4236/graphene.2017.61001>.
41. Vatanpour, V.; Madaeni, S.S.; Moradian, R.; Zinadini, S.; Astinchap, B. Fabrication and characterization of novel antifouling nanofiltration membrane prepared from oxidized multiwalled carbon nanotube/polyethersulfone nanocomposite. *J. Membr. Sci.* **2011**, *375*, 284–294. <https://doi.org/10.1016/j.memsci.2011.03.055>.
42. Li, X.; Fang, X.; Pang, R.; Li, J.; Sun, X.; Shen, J.; Han, W.; Wang, L. Self-assembly of TiO₂ nanoparticles around the pores of PES ultrafiltration membrane for mitigating organic fouling. *J. Membr. Sci.* **2014**, *467*, 226–235. <https://doi.org/10.1016/j.memsci.2014.05.036>.
43. Wang, H.H.; Jung, J.T.; Kim, J.F.; Kim, S.; Drioli, E.; Lee, Y.M. A novel green solvent alternative for polymeric membrane preparation via nonsolvent-induced phase separation (NIPS). *J. Membr. Sci.* **2018**, *574*, 44–54. <https://doi.org/10.1016/j.memsci.2018.12.051>.
44. Maggay, I.V.; Yu, M.-L.; Wang, D.-M.; Chiang, C.-H.; Chang, Y.; Venault, A. Strategy to prepare skin-free and macrovoid-free polysulfone membranes via the NIPS process. *J. Membr. Sci.* **2022**, *655*, 120597. <https://doi.org/10.1016/j.memsci.2022.120597>.
45. Liu, C.; Zhang, L.; Liu, R.; Gao, Z.; Yang, X.; Tu, Z.; Yang, F.; Ye, Z.; Cui, L.; Xu, C.; et al. Hydrothermal synthesis of N-doped TiO₂ nanowires and N-doped graphene heterostructures with enhanced photocatalytic properties. *J. Alloy. Compd.* **2016**, *656*, 24–32. <https://doi.org/10.1016/j.jallcom.2015.09.211>.
46. Chen, W.; Su, Y.; Zhang, L.; Shi, Q.; Peng, J.; Jiang, Z. In situ generated silica nanoparticles as pore-forming agent for enhanced permeability of cellulose acetate membranes. *J. Membr. Sci.* **2009**, *348*, 75–83. <https://doi.org/10.1016/j.memsci.2009.10.042>.
47. Wu, H.; Mansouri, J.; Chen, V. Silica nanoparticles as carriers of antifouling ligands for PVDF ultrafiltration membranes. *J. Membr. Sci.* **2013**, *433*, 135–151. <https://doi.org/10.1016/j.memsci.2013.01.029>.
48. He, J.; Xiong, D.; Zhou, P.; Xiao, X.; Ni, F.; Deng, S.; Shen, F.; Tian, D.; Long, L.; Luo, L. A novel homogenous in-situ generated ferrihydrite nanoparticles/polyethersulfone composite membrane for removal of lead from water: Development, characterization, performance and mechanism. *Chem. Eng. J.* **2020**, *393*, 124696.
49. Janković, I.A.; Šaponjić, Z.V.; Čomor, M.I.; Nedeljković, J.M. Surface Modification of Colloidal TiO₂ Nanoparticles with Bidentate Benzene Derivatives. *J. Phys. Chem. C* **2009**, *113*, 12645–12652. <https://doi.org/10.1021/jp9013338>.
50. Guillen, G.R.; Pan, Y.; Li, M.; Hoek, E.M.V. Preparation and Characterization of Membranes Formed by Nonsolvent Induced Phase Separation: A Review. *Ind. Eng. Chem. Res.* **2011**, *50*, 3798–3817. <https://doi.org/10.1021/ie101928r>.
51. Yang, Y.; Wang, P. Preparation and characterizations of a new PS/TiO₂ hybrid membranes by sol–gel process. *Polymer* **2006**, *47*, 2683–2688. <https://doi.org/10.1016/j.polymer.2006.01.019>.
52. Zambare, R.S.; Dhopte, K.B.; Patwardhan, A.V.; Nemade, P.R. Polyamine functionalized graphene oxide polysulfone mixed matrix membranes with improved hydrophilicity and anti-fouling properties. *Desalination* **2017**, *403*, 24–35. <https://doi.org/10.1016/j.desal.2016.02.003>.
53. Vatanpour, V.; Madaeni, S.S.; Rajabi, L.; Zinadini, S.; Derakhshan, A.A. Boehmite nanoparticles as a new nanofiller for preparation of antifouling mixed matrix membranes. *J. Membr. Sci.* **2012**, *401–402*, 132–143. <https://doi.org/10.1016/j.memsci.2012.01.040>.

54. Ikhsan, S.N.W.; Yusof, N.; Aziz, F.; Misdan, N.; Ismail, A.F.; Lau, W.-J.; Jaafar, J.; Salleh, W.N.W.; Hairom, N.H.H. Efficient separation of oily wastewater using polyethersulfone mixed matrix membrane incorporated with halloysite nanotube-hydrous ferric oxide nanoparticle. *Sep. Purif. Technol.* **2018**, *199*, 161–169. <https://doi.org/10.1016/j.seppur.2018.01.028>.
55. Wienk, I.M.; Van, D.; Boomgaard, T.; Smolders, C.A. The formation of nodular structures in the top layer of ultrafiltration membranes. *J. Appl. Polym. Sci.* **1994**, *53*, 1011–1023.
56. Wienk, I.M.; Boom, R.M.; Beerlage, M.A.M.; Bulte, A.M.W.; Smolders, C.A.; Strathmann, H. Recent advances in the formation of phase inversion membranes made from amorphous or semi-crystalline polymers. *J. Membr. Sci.* **1996**, *113*, 361–371. [https://doi.org/10.1016/0376-7388\(95\)00256-1](https://doi.org/10.1016/0376-7388(95)00256-1).
57. Wang, P.; Ma, J.; Wang, Z.; Shi, F.M.; Liu, Q.L. Enhanced separation performance of PVDF/PVP-g-MMT nanocomposite ultrafiltration membrane based on the NVP-grafted polymerization modification of montmorillonite (MMT). *Langmuir* **2012**, *28*, 4776–4786.
58. Teow, Y.H.; Ooi, B.S.; Ahmad, A.L. Fouling behaviours of PVDF-TiO₂ mixed-matrix membrane applied to humic acid treatment. *J. Water Process Eng.* **2017**, *15*, 89–98.
59. Yuan, X.-T.; Xu, C.-X.; Geng, H.-Z.; Ji, Q.; Wang, L.; He, B.; Jiang, Y.; Kong, J.; Li, J. Multifunctional PVDF/CNT/GO mixed matrix membranes for ultrafiltration and fouling detection. *J. Hazard. Mater.* **2020**, *384*, 120978. <https://doi.org/10.1016/j.jhazmat.2019.120978>.
60. Jhaveri, J.H.; Patel, C.M.; Murthy, Z.V.P. Preparation, characterization and application of GO-TiO₂/PVC mixed matrix membranes for improvement in performance. *J. Ind. Eng. Chem.* **2017**, *52*, 138–146.
61. Zinadini, S.; Rostami, S.; Vatanpour, V.; Jalilian, E. Preparation of antibiofouling polyethersulfone mixed matrix NF membrane using photocatalytic activity of ZnO/MWCNTs nanocomposite. *J. Membr. Sci.* **2017**, *529*, 133–141. <https://doi.org/10.1016/j.memsci.2017.01.047>.
62. Rajabi, H.; Ghaemi, N.; Madaeni, S.S.; Darael, P.; Astinchap, B.; Zinadini, S.; Razavizadeh. Nano-ZnO embedded mixed matrix polyethersulfone (PES) membrane: Influence of nanofiller shape on characterization and fouling resistance. *Appl. Surf. Sci.* **2015**, *349*, 66–77.
63. Mukherjee, R.; Bhunia, P.; De, S. Impact of graphene oxide on removal of heavy metals using mixed matrix membrane. *Chem. Eng. J.* **2016**, *292*, 284–297. <https://doi.org/10.1016/j.cej.2016.02.015>.
64. Hwang, K.-J.; Sz, P.-Y. Effect of membrane pore size on the performance of cross-flow microfiltration of BSA/dextran mixtures. *J. Membr. Sci.* **2011**, *378*, 272–279. <https://doi.org/10.1016/j.memsci.2011.05.018>.
65. Xu, Z.; Ye, X.; Hu, P.; Min, Y.A.; Bosheng, L.V.; Qin, M.B.; Gao, C. Azido-group functionalized graphene oxide/polysulfone mixed matrix ultrafiltration membrane with enhanced interfacial compatibility for efficient water and wastewater treatment. *Sep. Purif. Technol.* **2022**, *283*, 120162.
66. Ismail, R.A.; Kumar, M.; Thomas, N.; An, A.K.; Arafat, H.A. Multifunctional hybrid UF membrane from poly(ether sulfone) and quaternized polydopamine anchored reduced graphene oxide nanohybrid for water treatment. *J. Membr. Sci.* **2021**, *639*, 119779. <https://doi.org/10.1016/j.memsci.2021.119779>.
67. Zambare, R.S.; Dhopte, K.B.; Nemade, P.R.; Tang, C.Y. Effect of oxidation degree of GO nanosheets on microstructure and performance of polysulfone-GO mixed matrix membranes. *Sep. Purif. Technol.* **2020**, *244*, 116865. <https://doi.org/10.1016/j.seppur.2020.116865>.
68. Ma, H.; Xie, Q.; Wu, C.; Shen, L.; Hong, Z.; Zhang, G.; Lu, Y.; Shao, W. A facile approach to enhance performance of PVDF-matrix nanocomposite membrane via manipulating migration behavior of graphene oxide. *J. Membr. Sci.* **2019**, *590*, 117268. <https://doi.org/10.1016/j.memsci.2019.117268>.
69. Luque-Alled, J.M.; Abdel-Karim, A.; Alberto, M.; Leaper, S.; Perez-Page, M.; Huang, K.; Vijayaraghavan, A.; El-Kalliny, A.S.; Holmes, S.M.; Gorgojo, P. Polyethersulfone membranes: From ultrafiltration to nanofiltration via the incorporation of APTS functionalized-graphene oxide. *Sep. Purif. Technol.* **2020**, *230*, 115836. <https://doi.org/10.1016/j.seppur.2019.115836>.
70. Abdel-Karim, A.; Leaper, S.; Alberto, M.; Vijayaraghavan, A.; Fan, X.; Holmes, S.M.; Souaya, E.R.; Badawy, M.I.; Gorgojo, P. High flux and fouling resistant flat sheet polyethersulfone membranes incorporated with graphene oxide for ultrafiltration applications. *Chem. Eng. J.* **2018**, *334*, 789–799. <https://doi.org/10.1016/j.cej.2017.10.069>.
71. Farahani, M.H.D.A.; Vatanpour, V. A comprehensive study on the performance and antifouling enhancement of the PVDF mixed matrix membranes by embedding different nanoparticulates: Clay, functionalized carbon nanotube, SiO₂ and TiO₂. *Sep. Purif. Technol.* **2018**, *197*, 372–381. <https://doi.org/10.1016/j.seppur.2018.01.031>.
72. Arockiasamy, D.L.; Alhoshan, M.; Alam, J.; Muthumareeswaran; Figoli, A.; Kumar, S.A. Separation of proteins and antifouling properties of polyphenylsulfone based mixed matrix hollow fiber membranes. *Sep. Purif. Technol.* **2016**, *174*, 529–543. <https://doi.org/10.1016/j.seppur.2016.10.040>.
73. Zhang, J.; Wang, Z.; Wang, Q.; Pan, C.; Wu, Z. Comparison of antifouling behaviours of modified PVDF membranes by TiO₂ sols with different nanoparticle size: Implications of casting solution stability. *J. Membr. Sci.* **2016**, *525*, 378–386. <https://doi.org/10.1016/j.memsci.2016.12.021>.
74. Safarpour, M.; Khataee, A.; Vatanpour, V. Effect of reduced graphene oxide/TiO₂ nanocomposite with different molar ratios on the performance of PVDF ultrafiltration membranes. *Sep. Purif. Technol.* **2014**, *140*, 32–42. <https://doi.org/10.1016/j.seppur.2014.11.010>.

75. Padaki, M.; Emadzadeh, D.; Masturra, T.; Ismail, A. Antifouling properties of novel PSf and TNT composite membrane and study of effect of the flow direction on membrane washing. *Desalination* **2015**, *362*, 141–150. <https://doi.org/10.1016/j.desal.2015.01.012>.
76. Subramaniam, M. N.; Goh, P. S.; Lau, W. J.; Tan, Y. H.; Ng, B. C.; Ismail, A. F. Hydrophilic hollow fiber PVDF ultrafiltration membrane incorporated with titanate nanotubes for decolourization of aerobically-treated palm oil mill effluent. *Chem. Eng. J.* **2017**, *316*, 101–110.

Disclaimer/Publisher's Note: The statements, opinions and data contained in all publications are solely those of the individual author(s) and contributor(s) and not of MDPI and/or the editor(s). MDPI and/or the editor(s) disclaim responsibility for any injury to people or property resulting from any ideas, methods, instructions or products referred to in the content.